ACS APPLIED MATERIALS & INTERFACES

www.acsami.org

Research Article

Coordination Engineering Induced d-Band Center Shift on Single-Atom Fe Electrocatalysts for Enhanced Oxygen Reduction

Huimin Liu, Chen Wang, Chang Liu, Xing Zong, Yongfei Wang,* Xiaoxi Huang,* Zhizhi Hu, and Zhiqiang Zhang*

Cite This: https://doi.org/10.1021/acsami.3c03546

Read Online

ACCESS | Metrics & More | Article Recommendations | Supporting Information

ABSTRACT: Part of the performance of single-atom catalysts (SACs) is greatly influenced by the microenvironment around a single metal site, of which the oxygen reduction reaction (ORR) is counted as one of them. However, an in-depth understanding of the catalytic activity regulation by the coordination environment is still lacking. In this study, a single Fe active center with axial fifth hydroxyl (OH) and asymmetric N,S coordination embedded in a hierarchically porous carbon material (Fe-SNC) are prepared. Compared to Pt/C and most of the reported SACs, as-prepared Fe-SNC has certain advantages in terms of ORR activity and maintains sufficient stability. Furthermore, the assembled rechargeable Zn−air battery exhibits impressive performance. The combination of multiple findings revealed that the introduction of S atoms not only facilitates the formation of porous structures but also facilitates the desorption and adsorption of oxygen intermediates. On the other hand, with the introduction of axial OH groups, the bonding strength of the ORR intermediate is reduced, and even the central position of the Fe d-band is optimized. The developed catalyst is expected to lead to further research on the multiscale design of the electrocatalyst microenvironment.

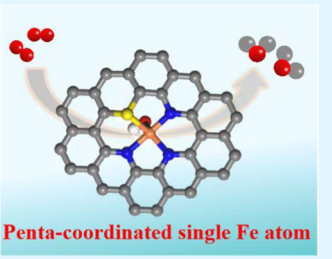

KEYWORDS: *single-atom catalysts, microenvironment modulation, penta-coordinated configuration, oxygen reduction reaction, Zn−air batteries*

1. INTRODUCTION

Peak carbon dioxide emissions and carbon neutrality are the major strategies mandated for successfully constructing a community with a shared future for humans. Development of novel energy-storage technology is key to achieving the "double carbon" goal.[1] In recent years, owing to advantages such as a high safety factor, cost effectiveness, and a high energy density, rechargeable zinc−air batteries have attracted immense attention from universities and enterprises.[2,3] Their energy conversion efficiency depends considerably on the cathodic oxygen reduction reaction (ORR). One of the issues is the slow kinetics of the ORR process.[4,5] Development of high-performance ORR electrocatalysts is clearly the key to promoting this process. Thus far, Pt-based materials are the most advanced and commercialized ORR catalysts. However, low ore reserves and high costs limit their wide range and large-scale applications.[6,7] In this context, it is crucial to explore Pt-group-metal-free-based ORR electrocatalysts with cost effectiveness and high performance.

Owing to their high activity and maximum atom utilization efficiency, single-atom catalysts (SACs) are also known as the most promising alternatives to Pt-based electrocatalysts.[8−10] Based on the current premise, among metal−nitrogen−carbon SACs, Fe−N−C has the highest efficiency in the ORR reaction process.[11] It is proved by theoretical derivation and calculations that the active center of an Fe−N−C catalyst is a symmetrical square-planar Fe−N_4 site.[12,13] As N exhibits strong electronegativity, not only will the free energy required for the mutual reaction of substances increase but also its electronegativity will interfere with the electronic properties of the metal active center, resulting in the limited improvement of catalyst reactivity.[14,15] This problem can be solved to a certain extent by adjusting the microenvironment of the active center.[16,17] Several studies reported that the introduction of heteroatoms (B, S, etc.) into the metal−nitrogen−carbon (Fe−N−C) catalyst improves the ORR performance, which can significantly optimize the microenvironment of the metal active center.[18−20] For example, Wang et al. employed a template method to synthesize the Fe SA-NSC-900 catalyst, which was mainly composed of atomically dispersed FeN_3S sites.[15] The introduction of S can induce charge redistribution, thereby reducing the energy barrier for the intermediates and accelerating reaction kinetics. Zhang et al. also reported a S-doped Fe−N−C catalyst with a 3D conductive stripped flake structure, indicating that doping with S can optimize the microenvironment via the change in the charge and spin distribution of catalysts.[21] The axial ligand effect is an

Received: March 11, 2023
Accepted: May 24, 2023

interesting and vital phenomenon in the ORR process; i.e., the $Fe(OH)N_4$ and $Fe-O-N_4$ active groups exist in Fe−N−C catalysts.[22,23] By adjusting the axial fifth ligand, the electronic structure of the central atom can be changed to a certain extent, and the result is to reduce the binding effect between the Fe center and the intermediate. A concerning factor is that the axial ligand is also part of the active center.[24,25] Therefore, the catalyst exhibits excellent performance. However, significant improvement in the ORR performance is difficult by using only one of the above-mentioned optimization strategies, and owing to the limited synthesis methods, the design of a penta-coordinated Fe center is a challenging study, especially with the provision of axial ligands and asymmetrical atomic interface.

Herein, we combine the above two optimization strategies and synthesize Fe SACs with asymmetric N, S, and axial fifth OH coordination (Fe-SNC) using an in situ self-sacrificial template method. Advanced characterization revealed that the active sites of Fe-SNC are atomically dispersed $Fe-N_3SOH$; that is, there are one axial OH group, one S atom, and three N atoms coordinated to the iron atom. The as-prepared catalyst exhibits a hierarchically porous architecture, which is beneficial for the exposure of a high number of active sites to achieve superior ORR activity. In a 0.1 M KOH electrolyte, the Fe-SNC catalyst exhibits a more positive half-wave potential ($E_{1/2}$) of 0.92 V and an ultralow Tafel value of 31 mV dec^{-1}, which surpass those of Pt/C and previously reported transition-metal-based SACs. Furthermore, a Zn−air battery, whose cathode catalyst component is Fe-SNC, shows certain advantages in terms of stability and peak power density. Density functional theory (DFT) calculations indicated that the introduction of S can effectively adjust the local charge density distribution of the iron atom sites, while the axial OH ligand plays a key role in reducing the d-band center of Fe and the adsorption−desorption of the O intermediate in ORR. This study provides insights into the relationship between the microenvironment of the metal center and electrocatalysis performance.

2. EXPERIMENTAL SECTION

2.1. Materials. Melamine ($C_3H_6N_6$), L-cysteine ($C_3H_7NO_2S$), iron(III) nitrate nonahydrate ($Fe(NO_3)_3{\cdot}9H_2O$), D(+)-glucose ($C_6H_{12}O_6$), and ethanol (C_2H_5OH) were obtained from Sinopharm Chemical Reagent Co. Ltd., China. Pt/C (20 wt %) was supplied by Sigma-Aldrich. All reagents were obtained without further purification.

2.2. Preparation of Materials. First, 10 g of melamine and 0.2 g of L-cysteine were dispersed in 20 mL of ethanol followed by vigorous stirring for 24 h. Then, the resulting powder was heat-treated at 550 °C for 4 h in a muffle furnace. Subsequently, the ground product (1 g), $C_6H_{12}O_6$ (0.12 mg), and $Fe(NO_3)_3{\cdot}9H_2O$ (0.024 g) were mixed into deionized water (40 mL). After ultrasonic and stirring treatment, evaporation is carried out to remove water. Finally, the as-obtained solid was pyrolyzed for 1 h at 900 °C under a nitrogen atmosphere. After cooling down to room temperature, the final product was synthesized, named Fe-SNC. For comparison, the same process was used for the synthesis of Fe-NC, SNC, and NC (for Fe-NC, no sulfur source were added; for SNC, no metal salts was added; for NC, no sulfur source and metal salts were added).

2.3. Structural Characterizations. The powder X-ray diffraction (XRD) patterns were obtained by a Bruker D8 X-ray diffractometer (Cu Kα radiation; λ = 1.5418 Å). The Raman spectra were characterized by a Bruker spectrometer with a 532 nm laser source. Scanning electron microscopy (SEM, FEI Magellan 400 XHR) and transmission electron microscopy (TEM, JEM-2100F) were used to detect the morphology of as-prepared samples. High-angle annular dark-field scanning transmission electron microscopy (HAADF-STEM) and energy-dispersive X-ray spectroscopy (EDX) were performed on a JEMARM200F instrument operating at 200 kV. The N_2 adsorption−desorption isotherms were measured at 77 K on a Quantachrome Instrument (Quantachrome Instruments Version 4.00). Inductively coupled plasma-optical emission spectrometry (ICP-OES) was conducted on an IRIS Intrepid II XSP instrument. X-ray photoelectron spectroscopy (XPS) spectra were measured using an AXIS Supra system (Kratos, U.K.) equipped with an Al Kα radiation source. The X-ray absorption fine structure spectra (XAFS; Fe K-edge) were collected at the 4B9A beamline in Beijing Synchrotron Radiation Facility (BSRF). The storage rings of BSRF were operated at 2.5 GeV with a stable current of 400 mA. Using a Si(111) double-crystal monochromator, data collection was carried out in transmittance mode by a Lytle detector. All spectra were collected in ambient conditions. The position of the absorption edge (E_0) of all data was seriously calibrated using Fe foil. The acquired data were analyzed according to the standard procedures using Athena and Artemis software.

2.4. Electrochemical Tests. The electrochemical performance of the catalyst was tested on a CHI 760E workstation by a traditional three-electrode system. The catalyst supported on a rotating ring disk electrode (RRDE, $A_{\text{glassy carbon}}$ = 0.1256 cm^2, $A_{\text{Pt-ring}}$ = 0.1884 cm^2) or rotating disk electrode (RDE, $A_{\text{glassy carbon}}$ = 0.196 cm^2) was used as the working electrode. The counter electrode and reference electrode were Pt mesh and Ag/AgCl (3.5 M KCl), respectively. The measured versus Ag/AgCl potential was converted into reversible hydrogen electrode (RHE) potential according to the Nernst equation ($E = E_0 + E_{\text{Ag/AgCl}} + 0.059^*$ pH − IRs).[3] To prepare the working electrode, 2.5 mg of catalysts were dispersed in 490 μL of ethanol, 490 μL of deionized water, and 20 μL of Nafion solution and sonicated for 30 min to form a homogeneous ink. Then, 5.4 or 8.3 μL of ink was dropped onto the RRDE or RDE to get a 0.105 mg cm^{-2} loading amount. A Pt/C (20 wt % of Pt) catalyst with the same loading was used as a reference. The ORR performances were tested in a O_2- or N_2-saturated 0.1 M KOH solution. Linear sweep voltammetry (LSV) was used to test the polarization at different rotating speeds from 100 to 1600 rpm. The electrochemical impedance spectroscopy (EIS) test was carried out in the frequency range from 100 kHz to 0.01 Hz by applying 0.1 V amplitude. The electrochemical double-layer capacitance (C_{dl}) was determined by measuring the scan-rate dependence of CV. The stability test was performed by chronopotentiometry at a constant current density (0.1 mA cm^{-2}).

2.5. Assembly of Zn−Air Batteries. The Zn−air battery performances were measured by a CT3001A battery testing system (Wuhan Landian Electronics Co. Ltd., China) in an aqueous solution of 6.0 M KOH and 0.2 M $ZnCl_2$ using a Zn plate as an anode and self-made catalyst ink supported on a carbon paper (A_{covered} = 0.2 cm^2, loading mass = 0.21 mg cm^{-2}) as a cathode.

2.6. Density Functional Theory (DFT) Calculation Methods. DFT calculations were performed using the MedeA Vienna ab-initio simulation package (VASP) with Generalized Gradient Approximation Perdew−Burke−Ernzerhof (GGA-PBE) as the exchange−correlation functional.[26−29] The plane wave cutoff energy was set at 400 eV. A graphene supercell with 6 × 6 × 1 periodicity was used as a basis to construct the single Fe structures. The vacuum height was set at 20 Å perpendicular to the slab. The 2 × 2 × 1 k-point mesh was used for the calculation. All atoms were allowed to relax during structural optimization. Also, the convergence criterion for energy and forces were set to 1 × 10^{-5} eV and 0.01 eV/Å, respectively. van der Waals interactions were involved by the DFT+D3 approach of Grimme with zero damping.[30] For electronic calculations, the k-points were sampled at 6 × 6 × 1. The correlation energy (U) and the exchange energy (J) were set at 4 eV and 1 eV for Fe 3d orbitals, respectively.[31]

For ORR reactions, the following four consecutive proton/electron transfer steps and the step of O_2 adsorption were considered.

$$^* + O_2 = {}^*O_2 \quad {}^* + O_2 = {}^*O_2$$

https://doi.org/10.1021/acsami.3c03546
ACS Appl. Mater. Interfaces XXXX, XXX, XXX−XXX

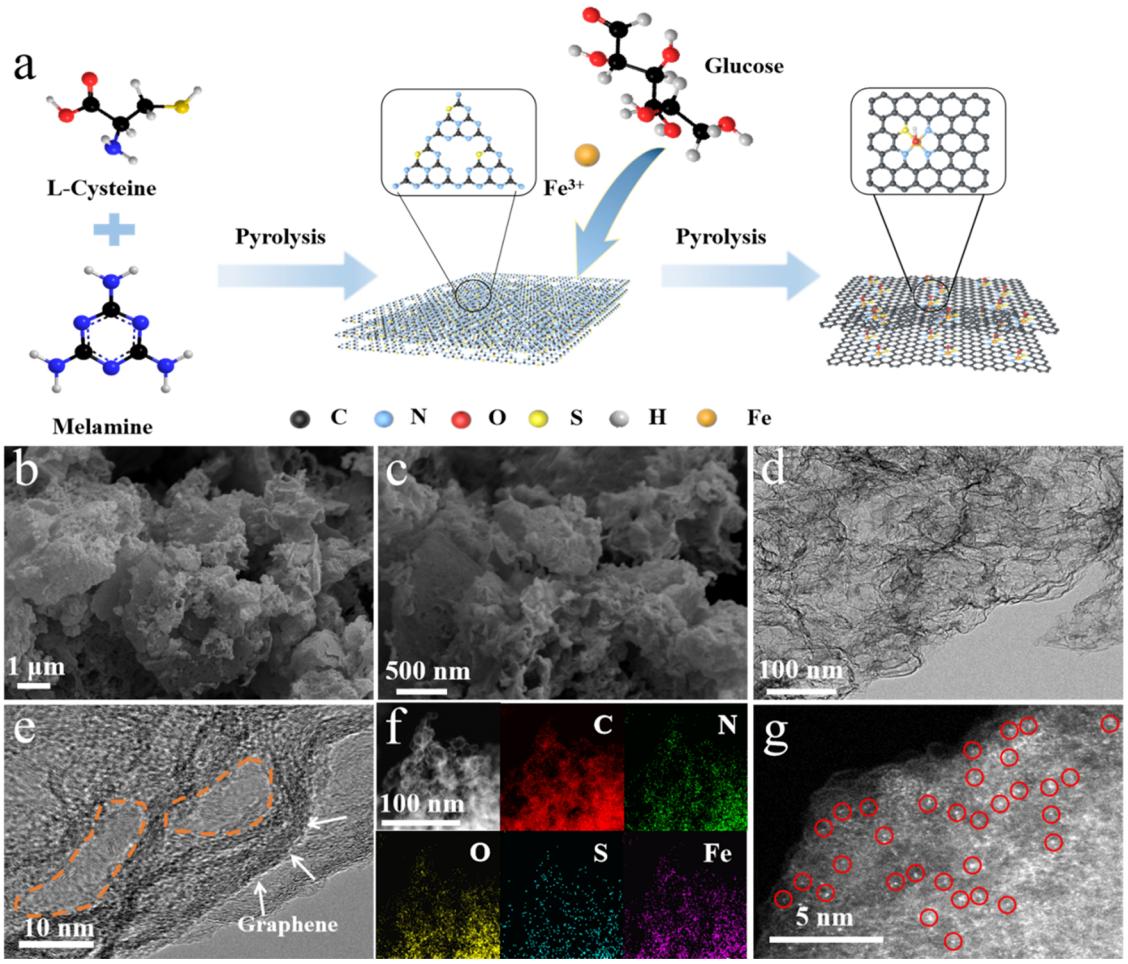

Figure 1. (a) Schematic of the synthesis process for Fe-SNC. (b, c) SEM images at different magnifications. (d) TEM image. (e) High-resolution TEM (HRTEM) image. (f) HAADF-STEM-related elemental mapping images and (g) HAADF-STEM image of Fe-SNC.

$$^{*}O_2 + (H^+ + e^-) = {}^{*}OOH$$

$$^{*}O_2 + H_2O + e^- = {}^{*}OOH + OH^-$$

$$^{*}OOH + (H^+ + e^-) = {}^{*}O + H_2O \text{ (acidic)} \qquad ^{*}OOH + e^- = {}^{*}O + OH^- \text{ (basic)}$$

$$^{*}O + (H^+ + e^-) = {}^{*}OH \qquad ^{*}O + H_2O + e^- = {}^{*}OH + OH^-$$

$$^{*}OH + (H^+ + e^-) = {}^{*} + H_2O \qquad ^{*}OH + e^- = {}^{*} + OH^-$$

Vaspkit was used for free energy correction of the adsorbed molecules.[32] The computational hydrogen electrode (CHE) model was used to describe the effect of electrical potential.[33]

3. RESULTS AND DISCUSSION

Figure 1a shows the synthetic route of Fe-SNC. First, SNC was obtained by the calcination of a certain amount of a mixture of L-cysteine and melamine. Second, $Fe(NO_3)_3{\cdot}9H_2O$ was used as the iron source, and it was mixed with the SNC suspension and glucose. Finally, the obtained solids were subjected to carbonization under 900 °C (Fe-SNC). The content of metals loaded on Fe-SNC was 8.93 wt % as measured by inductively coupled plasma-optical emission spectroscopy (ICP-OES), which was greater than those of most of the recently reported SACs. A high metal content can provide a high number of active sites. At the same time, it was beneficial to obtain more reliable signals in advanced characterization.

The prepared catalyst was tested by scanning electron microscopy (SEM), and its material morphology could be determined (Figures 1b,c and S1). Fe-NC comprised irregular sheets. After S doping, a large number of honeycomb pores were observed. Moreover, no metal particles were observed for Fe-SNC by transmission electron microscopy (TEM) (Figure 1d). The high-resolution TEM (HRTEM) image of Fe-SNC revealed numerous mesopore structures (orange cycles), which could improve mass transfer during the ORR process (Figure 1e).[3] In addition, the presence of mesopores was confirmed; that is, the nitrogen adsorption−desorption curves exhibited a type IV isotherm.[3,11] The unique structure endowed the Fe-SNC catalyst with a large specific surface area of 669.07 $m^2\ g^{-1}$, which is greater than that of Fe-NC (631.27 $m^2\ g^{-1}$). The corresponding pore-size distribution curves revealed that Fe-SNC is mainly enriched with mesopores and that its total pore volume of 5.47 $cm^3\ g^{-1}$ is greater than that of Fe-NC (2.94 $cm^3\ g^{-1}$) (Figure S2, Table S1). To confirm the existing form of Fe in the catalyst, aberration-corrected high-angle annular dark-field scanning transmission electron microscopy (HAADF-STEM) was used for detection. Metal atoms (bright spots) were uniformly dispersed in the carbon matrix, indicating that isolated Fe atoms are formed on the N,S co-doped carbon structure (Figure 1g). While the reference sample synthesized without the S dopant also revealed the presence of isolated Fe atoms, the distribution was not uniform (Figure S3), and the Fe loading (8.72 wt %) of Fe-NC was slightly less than that of

https://doi.org/10.1021/acsami.3c03546
ACS Appl. Mater. Interfaces XXXX, XXX, XXX−XXX

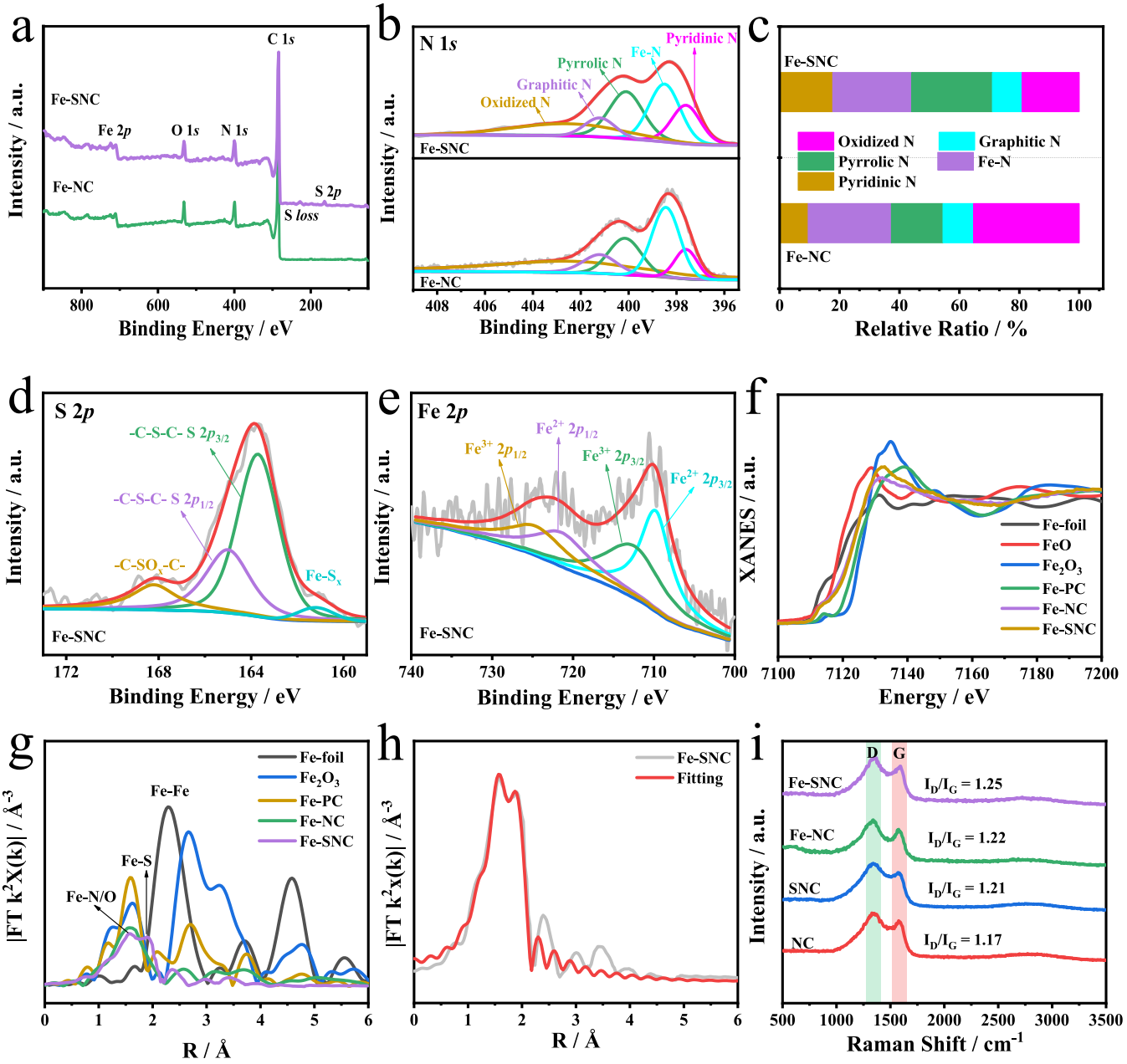

Figure 2. (a, b) XPS survey and high-resolution N 1 s spectrum of Fe-NC and Fe-SNC. (c) Relative content ratio of different N species in Fe-NC and Fe-SNC. High-resolution XPS (d) S 2p and (e) Fe 2p spectra of Fe-SNC. (f) Fe K-edge XANES and (g) FT Fe K-edge EXAFS spectra of Fe-SNC and reference samples. (h) FT-EXAFS *R*-space fitting curve of Fe-SNC. (i) Raman spectra of various catalysts.

Fe-SNC. This result was probably related to the anchoring of a high number of metal atoms by the doping of S. In addition, the energy-dispersive X-ray (EDX) spectrum in HAADF-STEM revealed a uniform distribution of C, N, O, S, and Fe over Fe-SNC (Figure 1f). X-ray diffraction (XRD) also suggested that the metal species are atomically dispersed on carbon materials (Figure S4). Only one broad peak was found in all of the tested samples, which was attributed to the (002) reflection of graphitized carbon.[34]

The local coordination and chemical composition of the sample can be analyzed and verified by X-ray photoelectron spectroscopy (XPS) detection technology. According to the XPS survey image (Figure 2a), S was doped into the carbon matrix. The high-resolution C 1s spectra of Fe-NC and Fe-NSC were split into C−C/C═C (284.4 eV), C−N/C−S (286 eV), and C═O species (288.9 eV). These results also confirmed that N and S exist in the support (Figure S5a).[35] In the high-resolution O 1s spectrum, an Fe−O bond was observed at 530.5 eV, confirming that the coordination between Fe and OH exists in Fe-SNC (Figure S5b).[36] In addition, in the N 1s spectrum shown in Figure 2b, the peaks of oxidized-*N*, pyrrolic-*N*, Fe−N, graphitic-*N*, and pyridinic-*N* were observed at 402.5 ± 0.1, 400.1 ± 0.1, 398.5 ± 0.1, 401.2 ± 0.1, and 397.6 ± 0.1 eV, respectively.[17] Notably, compared to Fe-NC, Fe-NSC exhibited the highest percentage of pyridinic-*N* and pyrrolic-*N* in all N species (Figure 2c and Table S2), which were favorable for the ORR process. This result is related to the capture of isolated Fe atoms by pyridine-*N* with lone-pair electrons, which is conducive to obtaining good activity and stability.[3,21] On the other hand, pyrrole-*N*,

https://doi.org/10.1021/acsami.3c03546
ACS Appl. Mater. Interfaces XXXX, XXX, XXX−XXX

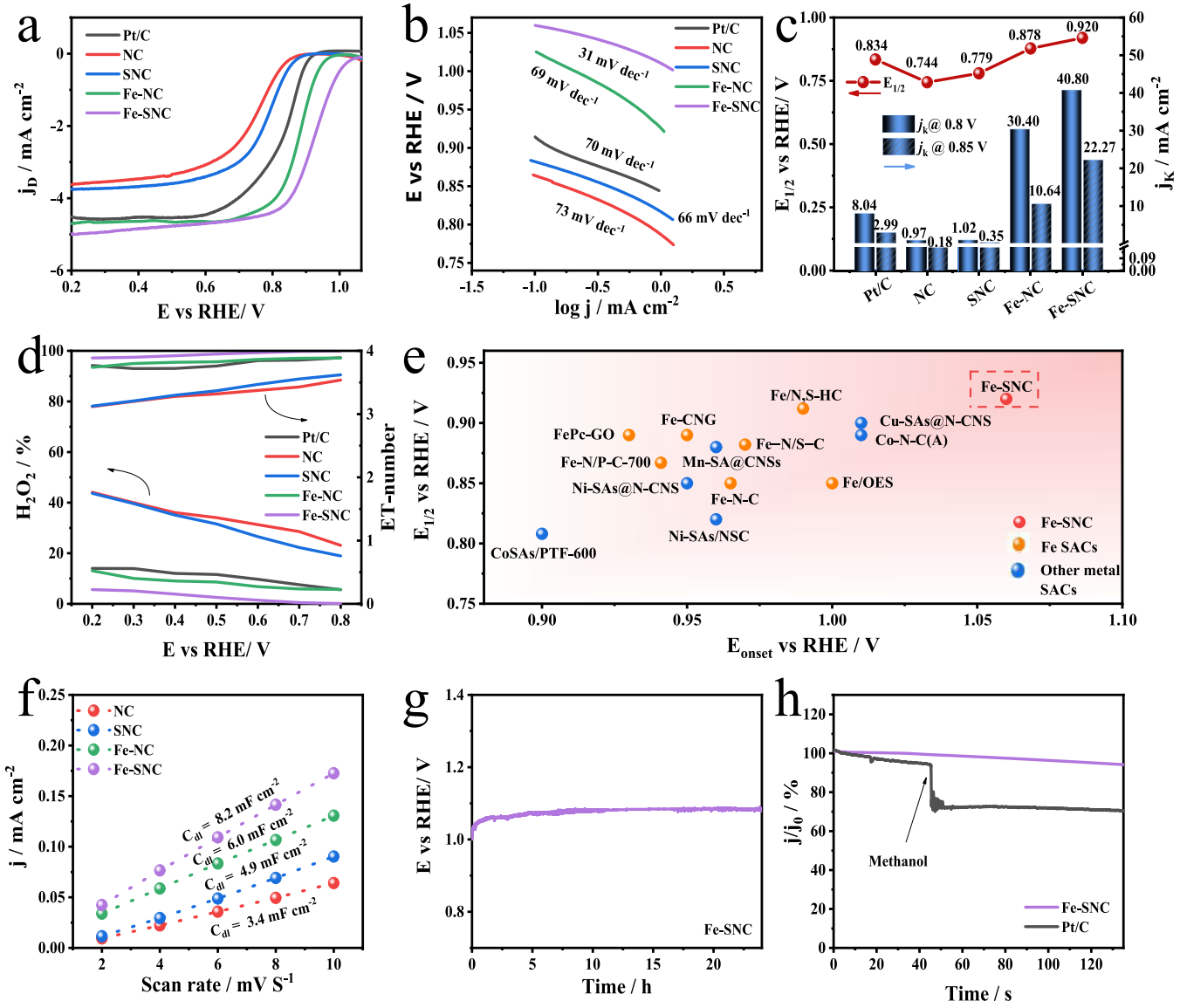

Figure 3. (a) LSV curves and (b) Tafel slopes of Fe-SNC and the control samples in 0.1 M KOH solution. (c) Contrast between Fe-SNC and the control samples for J_k (0.80, 0.85 V) and $E_{1/2}$. (d) H_2O_2 yield and electron transfer number (n) of the Fe-SNC and control samples. (e) Comparison of the E_{onset} and $E_{1/2}$ between Fe-SNC and the state-of-the-art Fe or other metal-based SACs reported recently. (f) Electrochemical double-layer capacitance of Fe-SNC and the control samples. (g) Long-term durability tests of Fe-SNC. (h) Methanol resistance test of Fe-SNC and Pt-C.

which was typically located in vacancy, can disrupt the π-orbital resonance and form a positive electron-rich state, resulting in increased catalyst reactivity.[21,37,38] In addition, some S atoms replaced N atoms, and a slight shift in the N 1s spectrum of Fe-NC was mainly observed.[3] The high-resolution S 2p spectrum of SNC revealed three characteristic peaks: C−S−C S $2p_{3/2}$ (163.7 eV), C−S−C S $2p_{1/2}$ (165 eV), and C−SO_x−C (168.2 eV), as shown in Figure S6. This result indicated that S mainly exists as C−S−C, confirming that S is mainly doped in the carbon matrix. In addition, an Fe−S_x bond (161.2 eV) was observed in Figure 2d, indicating that some S atoms coordinated with Fe and formed active sites.[21,35] According to the Fe 2p spectra (Figures 2e and S7), four peaks of Fe $2p_{1/2}$ (721.3 and 724.3 ± 0.2 eV) and Fe $2p_{3/2}$ (709.8 and 712.5 ± 0.2 eV) were observed.[39] Notably, the peak at 712.5 eV of Fe $2p_{3/2}$ confirmed possible coordination with pyridinic-*N* to form Fe−N_x sites in the catalyst.[40,41]

Analytical verification of prepared samples by extended X-ray absorption fine structure (EXAFS) and near-edge structure (XANES) allows for the secondary confirmation of the coordination environment. The absorption edges of Fe-SNC and Fe-NC were located between Fe_2O_3 and FeO, indicating that the valence states of Fe in catalysts are between +2 and +3, as shown in Figure 2f.[42,43] Two peaks were observed in the corresponding FT-EXAFS diagram of Fe-SNC (Figure 2g): One peak was located at ∼1.55 Å, corresponding to the Fe−N bond. The other peak was observed at ∼1.90 Å, corresponding to the common scattering path of Fe−S and Fe−O bonds.[3,15] Notably, the Fe−N peak position of Fe-SNC shifted slightly in comparison with that of Fe-NC (∼1.58 Å), which was probably related to the introduction of S.[35,44] In addition, according to the analysis of the Fe−Fe bond (∼2.2 Å) data, it can be concluded that the Fe−Fe bond does not exist and Fe atoms exist independently in Fe-SNC and Fe-NC, consistent

https://doi.org/10.1021/acsami.3c03546
ACS Appl. Mater. Interfaces XXXX, XXX, XXX−XXX

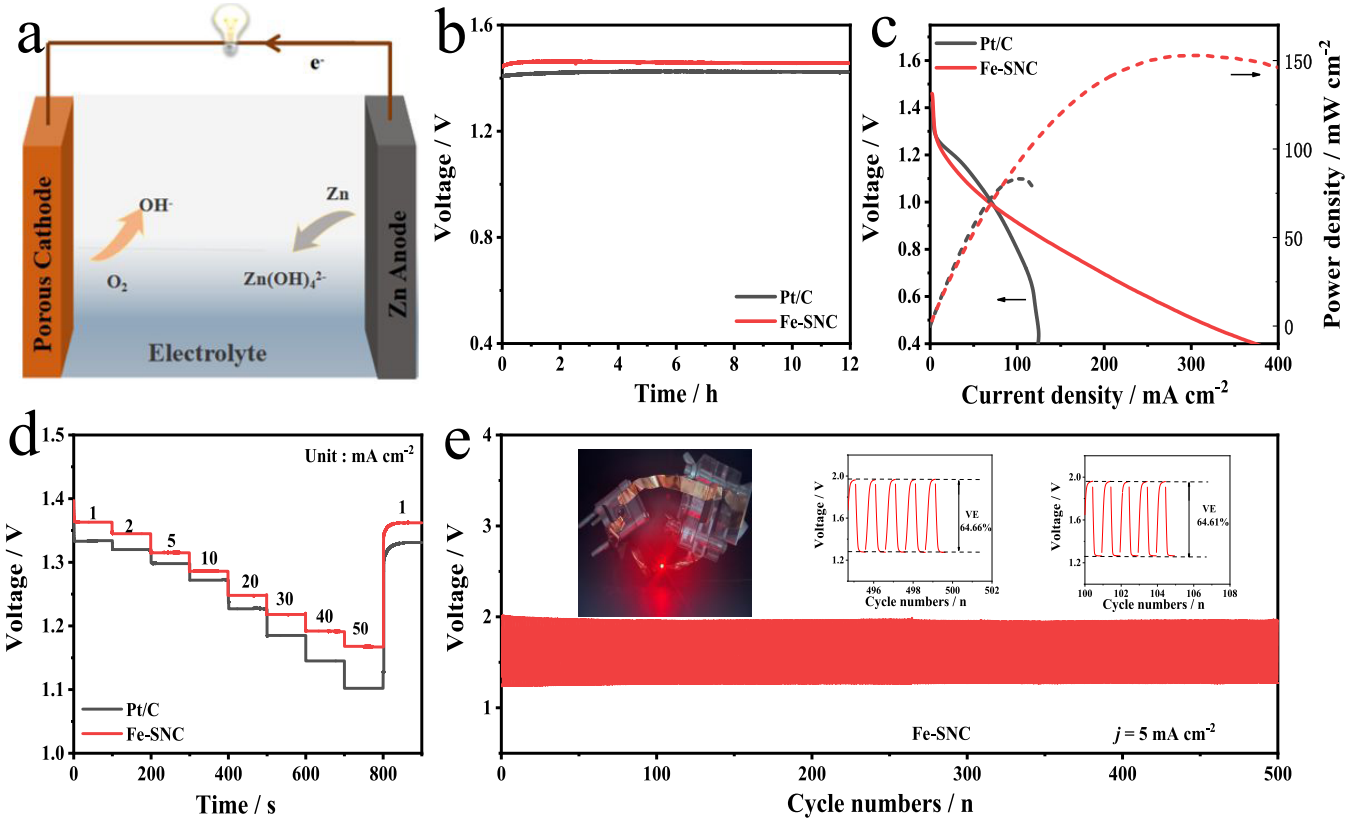

Figure 4. (a) Schematic illustration of the Zn−air battery. (b) Open-circuit potential (OCV) plots of Fe-SNC and Pt/C. (c) Polarization and power density curves. (d) Discharge curves of samples at different current densities. (e) Corresponding charge−discharge cycling performance of a Zn−air battery assembled with Fe-SNC. Inset: photo of a red LED powered by the assembled Fe-SNC-based Zn−air batteries and the voltage efficiency (VE) during the cycling test.

with the HAADF-STEM results.[45] Moreover, the precise confirmation of the central coordination structure of Fe in Fe-SNC was determined by EXAFS *k*-space and *R*-space fitting analysis (Figures 2h and S8). As displayed in Table S3, the number ratio of Fe atoms, N atoms, S atoms, and OH groups was 1:3:1:1, further confirming that the main active site is the FeN_3S_1OH structure formed in Fe-SNC. In addition, the presence of porous structures indicated that a high number of defects are present in Fe-SNC, which is confirmed by Raman spectra (Figure 2i). The I_D/I_G ratio for Fe-SNC (1.25) was significantly greater than those for Fe-NC (1.22), SNC (1.21), and NC (1.17), suggesting that S doping leads to the formation of a high number of defects.[46,47]

The ORR properties of the Fe-SNC and control samples were evaluated in a 0.1 M KOH solution. Fe-SNC exhibited excellent ORR performance as confirmed by the most positive onset potential (the voltage corresponding to the current density of −0.1 mA cm^{-2} (E_{onset}) = 1.06 V) and half-wave potentials ($E_{1/2}$, 0.92 V), greater than those of NC ($E_{1/2}$, 0.744 V), SNC ($E_{1/2}$, 0.779 V), and Fe-NC ($E_{1/2}$, 0.878 V), and even better than that of commercial Pt/C ($E_{1/2}$ = 0.834 V), as shown in Figures 3a and S9. Notably, compared to the Fe or other transition-metal-based SACs reported recently, it also exhibited better competitiveness (Figure 3e, Table S4). The Tafel plots revealed that Fe-SNC exhibits better ORR kinetics, with an ultralow Tafel value (31 mV dec^{-1}) in comparison with those of NC (73 mV dec^{-1}), SNC (66 mV dec^{-1}), Fe-NC (39 mV dec^{-1}), and commercial Pt/C (70 mV dec^{-1}) (Figure 3b). By calculating the kinetic current density (j_k) values at 0.85 and 0.8 V, the kinetic process can be further determined (Figure 3c). Fe-SNC exhibited a remarkable kinetic current density of 40.8 mA cm^{-2} at 0.8 V and 22.27 mA cm^{-2} at 0.85 V, which were considerably greater than those of commercial Pt/C (8.04 mA cm^{-2} at 0.8 V and 2.99 mA cm^{-2} at 0.85 V). The excellent Tafel value and kinetic current density revealed that the kinetic process for Fe-SNC is faster than that for Pt/C. The reaction path and H_2O_2 production during ORR were also examined (Figure 3d). By calculation, the average electron transfer number of Fe-SNC is ~3.95, the above data is the conclusion drawn in the whole potential range, and the H_2O_2 yield also exhibited the lowest range, indicating that Fe-SNC follows the four-electron path and exhibits excellent selectivity. Furthermore, Fe-SNC exhibited a small charge-transfer resistance, indicating that it exhibits the fastest reaction kinetics (Figure S10). The electrochemical double-layer capacitance (C_{dl}) value was proportional to the electrochemically active specific surface area (ECSA). The C_{dl} value of Fe-SNC was 8.2 mF cm^{-2}, which was considerably greater than those of Fe-NC (6 mF cm^{-2}), SNC (4.9 mF cm^{-2}), and NC (3.4 mF cm^{-2}), indicating that Fe-SNC catalysts expose more active specific surface area (Figures 3f and S11). These results are attributed to the presence of porous structures and FeN_3S_1OH active sites. Moreover, Fe-SNC exhibited the highest mass activity and turnover frequency (TOF) values of 43.5 mA cm^{-2} and 25.2 s^{-1} at 0.8 V, respectively (Figure S12), further indicative of excellent ORR activity. In addition, the durability and methanol tolerance of Fe-SNC were further investigated. During chronoamperometry tests, the initial

https://doi.org/10.1021/acsami.3c03546
ACS Appl. Mater. Interfaces XXXX, XXX, XXX−XXX

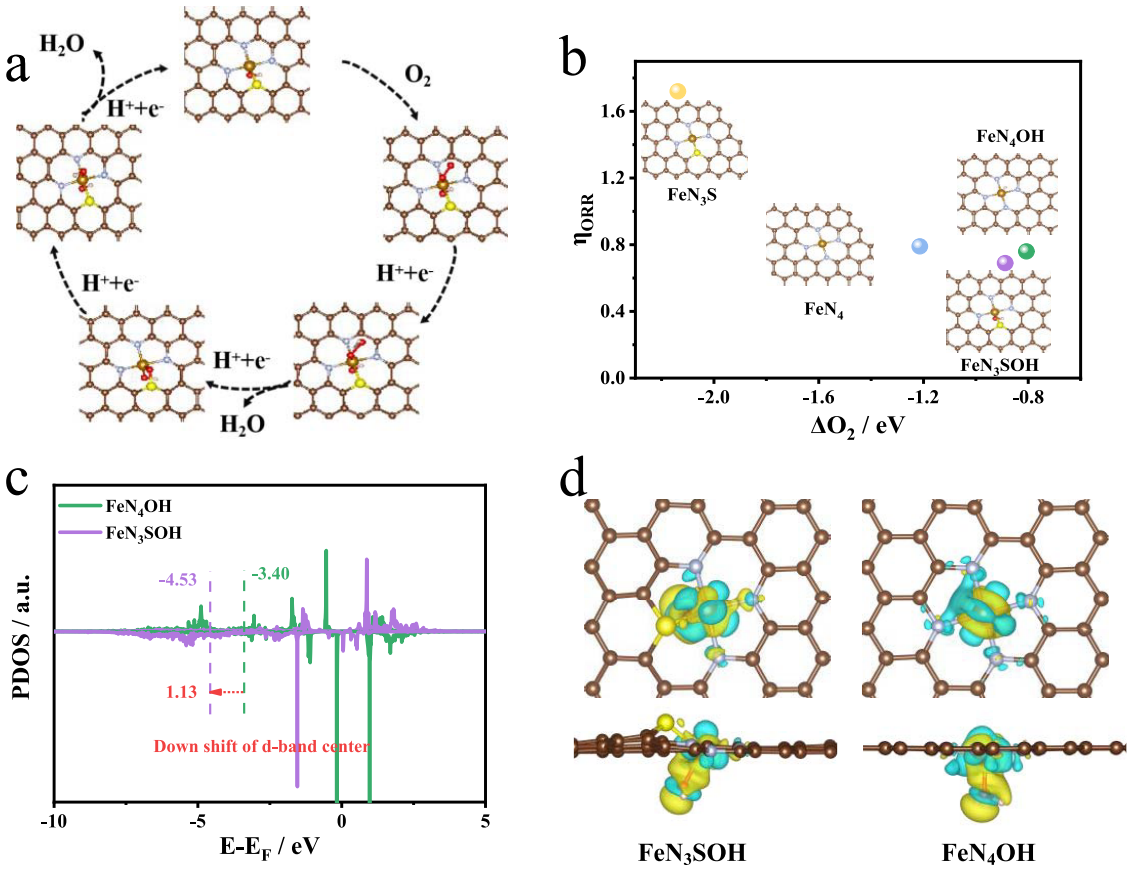

Figure 5. (a) Reaction pathway of ORR on Fe−N_3SOH. (b) Correlation of the ORR overpotentials with the O_2 adsorption free energy of different structural configurations. (c) d-band centers of FeN_4OH and FeN_3SOH moieties. (d) Charge density difference of Fe−N_3SOH and Fe−N_4OH.

current density almost did not change after 24 h (Figure 3g). It also exhibited excellent tolerance to methanol, as evidenced by the fact that Fe-SNC exhibits 94.2% retention of the initial activity in comparison with that of Pt/C after methanol injection (only 70% retention), as shown in Figure 3h. These results revealed that Fe-SNC demonstrates good potential for applications in energy conversion devices.

To obtain an in-depth understanding of the formation process of SACs, control variable experiments were performed, and control samples were prepared without the addition of glucose (Fe@NC and Fe@SNC). TEM results revealed that the metal in the samples prepared without glucose aggregates and exists as nanoparticles (NPs). At the same time, g-C_3N_4 exhibited a carbon nanotube structure (Figures S13 and S14). The reason for this phenomenon is that N atoms in g-C_3N_4 begin to evaporate and produce defect structures when the temperature is above 600 °C. Meanwhile, metal ions are reduced to metal NPs to adsorb defective carbon and serve as catalysts to promote the generation of carbon nanotubes, following the "reduction nucleation growth" mechanism.[8] Besides, g-C_3N_4 without any additives will completely decompose during the pyrolysis process, indicating that glucose contributes to the formation of carbon nanosheets. XPS spectra also demonstrated that Fe@NC and Fe@SNC contain metal NPs (Figure S15). Moreover, the survey spectra of Fe@SNC are presented in Figure S16, and no O 1s characteristic peak was observed, indicating that the origin of axial OH is closely related to glucose. Notably, compared to Fe-NC and Fe-SNC, Fe@NC and Fe@SNC exhibited poor ORR performance (Figure S17). These results suggested that glucose plays a key role in SAC formation; that is, glucose can be used as a chelating agent to fix metal atoms on g-C_3N_4, thereby effectively preventing metal atom aggregation.[8,48]

To further explore the practical applications of Fe-SNC for energy conversion and storage, the method adopted is to load Fe-SNC on carbon paper as the air cathode, zinc foil as the anode, and 6 M KOH containing 0.2 M $ZnCl_2$ as the electrolyte (Figure 4a). For comparison, a Zn−air battery was also assembled using Pt/C as the air cathode. The open-circuit voltage (OCV) of Pt/C was 1.43 V, which is lower than that of Fe-SNC based-zinc-air battery (1.457 V), being consistent with the conclusion obtained from the ORR test (Figure 4b). Besides, the Fe-SNC-based battery exhibited a peak power density of ∼152.9 mW cm^{-2}, which was greater than that of Pt/C (83.1 mW cm^{-2}) (Figure 4c). This result is related to the production of a high number of defects and the honeycomb structure by the doping of heteroatoms, thereby ensuring rapid mass transfer of Fe-SNC in the actual zinc−air battery device.[49−51] The specific capacity was obtained by galvanostatic discharge at a current density of 10 mA cm^{-2} (Figure S18), which exhibited a specific capacity of 802 mAh g^{-1}. As shown in Figure 4d, the discharge voltage of the Fe-SNC-based battery was significantly greater than that of the Pt/C-based battery under different current densities (1−50 mA cm^{-2}). Notably, when the current density reached 1 mA cm^{-2} again, the discharge voltage was almost the same as the original measured value, suggesting that Fe-SNC exhibits superior stability. Furthermore, it exhibited a quite stable and excellent performance in the long-term galvanostatic charge−discharge test at a current density of 5 mA cm^{-2}. After 100 cycles, the

https://doi.org/10.1021/acsami.3c03546
ACS Appl. Mater. Interfaces XXXX, XXX, XXX−XXX

energy efficiency ($E_{discharge}/E_{charge}$) of the battery was 64.6%, which was almost the same as that after 500 cycles (Figure 4e). To further confirm the stability of Fe-SNC catalysts, the morphology and microstructure of the catalyst after 500 cycles were characterized. SEM and HRTEM images for Fe-SNC revealed that the structure did not change significantly after the long-life galvanostatic charge−discharge test, underlining the excellent structural robustness (Figure S19). Notably, a red LED (2 V) could be powered for at least 80 h (Figure 4e). Overall, the performance of the Fe-SNC-based battery was superior to those of single-atom-based electrocatalysts reported currently (Table S5).

To explore the ORR kinetics mechanism and effect of the local coordination environment at the Fe atom for ORR, the structural models of FeN_4 and FeN_3S were employed for DFT calculations (Figure S20). Notably, FeN_4 and FeN_3S structures exhibited strong adsorption of oxygen species, which was not conducive to the last step of the desorption process, leading to poor ORR performance. Hence, the strong adsorption performance of the O intermediate demonstrates the high propensity of another axial O ligand to attach to Fe. Thus, the structural models of FeN_4OH and FeN_3SOH were established and investigated. First, the source of Fe-SNC's excellent ORR reactivity is determined by calculating the Gibbs free energy of each basic step of our model in ORR (Figure 5a). All of the elementary reaction pathways on FeN_4, FeN_3S, FeN_4OH, and FeN_3SOH were downhill at $U = 0$ V, corroborating exothermic reactions in ORR (Figure S20). In addition, at $U = 1.23$ V or the thermodynamic limiting potential, the intermediates on FeN_3SOH exhibited a weak binding energy, which was more conducive to the desorption of oxygen intermediates. Meanwhile, the last intermediate step was the rate-determining step of the overall ORR. Moreover, the judgment of electrocatalyst ORR performance is generally measured by the overpotential (η). Compared to FeN_4OH (0.76 V), FeN_4 (0.79 V), and FeN_3S (1.72 V), FeN_3SOH exhibited the lowest ORR potential (η_{ORR} = 0.69 V), which was close to that of Pt (111), as shown in Figure 5b.[20] Therefore, the introduction of FeN_3SOH coordination in the carbon matrix was confirmed to enhance ORR activity via the optimization of O_2 adsorption/activation, which coincides with the experimental results. Studies reported a close relationship between the d-band center of the metal and intermediate adsorption; hence, related calculations are conducted on the d-band electronic structure of the Fe center of all structures. Compared to FeN_4, FeN_3S, and FeN_4OH, FeN_3SOH was verified to considerably lower the d-band center to −4.53 eV (Figures 5c and S21). This result is related to the strong electron absorption ability of the axial OH ligand, which generates an additional transfer of charges; this additional charge transfer is conducive to achieving the best binding strength of ORR intermediates. However, the d-band center of FeN_3S was greater than that of FeN_4, revealing that only replacing N with S cannot enhance ORR activity. Compared with that of FeN_4OH, the distribution of differential charges of FeN_3SOH was broader, indicating that a larger number of electrons are induced to participate in the electron transition in FeN_3SOH, thereby realizing charge density redistribution (Figure 5d).[11,52]

Furthermore, the values of the projected density of states (PDOS) of Fe−N_3SOH and Fe−N_4OH were calculated, with significantly higher-density states near the Fermi level observed for the Fe−N_3SOH structures; this result indicated that partial S coordination leads to the high occupation of the valence orbitals, accelerating electron transfer (Figure S22). On the other hand, according to the PDOS analysis and calculation of Fe−N_4OH and Fe−N_3SOH, the 3d orbital of Fe mainly has the greatest influence on the DOS near the Fermi level. In addition, the interaction between the Fe 3d orbital and O p orbital was explained, the axial fifth OH group and the adjacent S were affected by the magnetic moment, and the conclusion could be drawn by calculating and analyzing the Fe center. Fe−N_3SOH exhibited several $3d_{yz}$ and $3d_z^2$ orbitals near the Fermi level before O_2 adsorption. Previously, oxygen adsorption was reportedly promoted by the formation of weak π bonds and strong σ bonds between the $3d_{yz}$ and $3d_z$ orbitals of the Fe and P orbitals of O.[3] This result is confirmed by Figure S20c. Clearly, the Fe $3d_z^2$ and $3d_{yz}$ orbitals for Fe−N_3SOH partially overlapped the O p orbital near the Fermi level, while the overlap of Fe−N_4OH was limited. Overall, DFT calculations confirmed that the asymmetric planar S and additional axial OH ligands could promote charge redistribution via the optimization of the electronic structure and that they play a synergistic role in accelerating ORR kinetics.

4. CONCLUSIONS

In summary, asymmetric N, S coordination and an axial OH ligand were successfully introduced into the Fe center, which were atomically dispersed and anchored on the porous carbon materials. Benefiting from the open hierarchical porous structure and well-designed coordination environment, Fe-SNC exhibited superior ORR activity and durability, surpassing Pt/C and several of the previously reported transition-metal-based SACs. Furthermore, Zn−air batteries equipped with Fe-SNC exhibited excellent performance compared to the Pt/C catalyst. Experimental and theoretical calculations demonstrated that the improved ORR reaction kinetics is attributed to the unique structure configuration (Fe−N_3SOH), which can adjust the charge distribution and enhance the adsorption and activation of O_2. This study revealed the necessity of reasonably designing and optimizing the microenvironment of single-atom catalysts (SACs) and provided new insights into the design of SACs for energy conversion and storage systems.

■ ASSOCIATED CONTENT

Supporting Information

The Supporting Information is available free of charge at https://pubs.acs.org/doi/10.1021/acsami.3c03546.

Additional characterization and electrochemical data, EDS spectra, N_2 adsorption/desorption isotherms, HADDF-STEM image, XRD patterns, high-resolution XPS spectra, EXAFS analysis, RRDE voltammograms, EIS plots, cyclic voltammograms, corresponding TOFs, TEM images, high-resolution Fe 2p spectra, XPS survey spectra, LSV curves and Tafel slopes, galvanostatic discharge curve, SEM and HRTEM images, free energy diagrams of ORR pathways, PDOS of Fe sites, and calculated PDOS of the Fe atoms (PDF)

■ AUTHOR INFORMATION

Corresponding Authors

Yongfei Wang − *School of Chemical Engineering, University of Science and Technology Liaoning, Anshan 114051, P. R. China; School of Materials and Metallurgy, University of Science and Technology Liaoning, Anshan, Liaoning 114051,*

https://doi.org/10.1021/acsami.3c03546
ACS Appl. Mater. Interfaces XXXX, XXX, XXX−XXX

P. R. China; orcid.org/0000-0003-3369-5518; Email: wyf8307@ustl.edu.cn

Xiaoxi Huang − *Hoffmann Institute of Advanced Materials, Shenzhen Polytechnic, Shenzhen 518055, P. R. China*; orcid.org/0000-0002-1975-2312; Email: xiaoxihuang@szpt.edu.cn

Zhiqiang Zhang − *School of Chemical Engineering, University of Science and Technology Liaoning, Anshan 114051, P. R. China*; Email: zzq@ustl.edu.cn

Authors

Huimin Liu − *School of Chemical Engineering, University of Science and Technology Liaoning, Anshan 114051, P. R. China*

Chen Wang − *School of Chemical Engineering, University of Science and Technology Liaoning, Anshan 114051, P. R. China*

Chang Liu − *School of Chemical Engineering, University of Science and Technology Liaoning, Anshan 114051, P. R. China*

Xing Zong − *School of Materials and Metallurgy, University of Science and Technology Liaoning, Anshan, Liaoning 114051, P. R. China*

Zhizhi Hu − *School of Chemical Engineering, University of Science and Technology Liaoning, Anshan 114051, P. R. China*

Complete contact information is available at: https://pubs.acs.org/10.1021/acsami.3c03546

Notes

The authors declare no competing financial interest.

■ ACKNOWLEDGMENTS

The authors gratefully acknowledge the financial support from the National Natural Science Foundation of China (Grant No. 21601076) and the Natural Science Foundation of Liaoning Province (No. 2019-ZD-0266).

■ REFERENCES

(1) Zhang, D. P.; Li, Y. X.; Li, Y.; Zhan, S. H. Towards single-atom photocatalysts for future carbon-neutral application. *SmartMat* **2022**, *3*, 417−446.

(2) Wang, Y.; Zheng, X.; Wang, D. Design concept for electrocatalysts. *Nano Res.* **2022**, *15*, 1730−1752.

(3) Li, L. B.; Huang, S. H.; Cao, R.; Yuan, K.; Lu, C. B.; Huang, B. Y.; Tang, X. N.; Hu, T.; Zhuang, X. D.; Chen, Y. W. Optimizing microenvironment of asymmetric N,S-coordinated single-atom Fe via axial fifth coordination toward efficient oxygen electroreduction. *Small* **2022**, *18*, 2105387−2105398.

(4) Liu, H. M.; Cheng, J. X.; Lu, Z. J.; Huang, X. N.; Zhu, Y. M.; Zhao, X. F.; Wang, T.; Masad, J.; Chen, X. X. Significant enhancement of the oxygen reduction activity of self-heteroatom doped coal derived carbon through oxidative pretreatment. *Electrochim. Acta* **2019**, *312*, 22−30.

(5) Gao, L. S.; Gao, X.; Jiang, P.; Zhang, C. Y.; Guo, H.; Cheng, Y. H. Atomically dispersed iron with densely exposed active sites as bifunctional oxygen catalysts for zinc-air flow batteries. *Small* **2022**, *18*, 2105892−2215901.

(6) Huang, B.; Wang, M. H.; Wu, C. X.; Guan, L. H. Highly dispersive metal atoms anchored on carbon matrix obtained by direct rapid pyrolysis of metal complexes. *CCS Chem.* **2022**, *43*, 2968−2979.

(7) Qin, J. Y.; Liu, H.; Zou, P. C.; Zhang, R.; Wang, C. Y.; Xin, H. L. Altering ligand fields in single-atom sites through second-shell anion modulation boosts the oxygen reduction reaction. *J. Am. Chem. Soc.* **2022**, *144*, 2197−2207.

(8) Wan, W. C.; Zha, Y. G.; Wei, S. Q.; Triana, C. A.; Li, J. G.; Arcifa, A.; Allen, C. S.; Cao, R.; Patzke, G. R. Mechanistic insight into the active centers of single/dual-atom Ni/Fe-based oxygen electrocatalysts. *Nat. Commun.* **2021**, *12*, No. 5589.

(9) Cui, T. T.; Wang, Y.-P.; Ye, T.; Wu, J.; Chen, Z. Q.; Li, J.; Lei, Y. P.; Wang, D. S.; Li, Y. D. Engineering dual single-atom sites on 2D ultrathin N-doped carbon nanosheets attaining ultra-low-temperature zinc-air battery. *Angew. Chem., Int. Ed.* **2022**, *61*, No. e202115219.

(10) Li, R.; Wang, D. Understanding the structure-performance relationship of active sites at atomic scale. *Nano Res.* **2022**, *15*, 6888−6923.

(11) Liu, J. J.; Gong, Z. C.; Allen, C.; Ge, W.; Gong, H. S.; Liao, J. W.; Liu, J. B.; Huang, K.; Yan, M. M.; Liu, R.; He, G. C.; Dong, J. C.; Ye, G. L.; Fei, H. L. Edge-hosted Fe-N_3 sites on a multiscale porous carbon framework combining high intrinsic activity with efficient mass transport for oxygen reduction. *Chem. Catal.* **2021**, *1*, 1291−1307.

(12) Chen, G. B.; An, Y.; Liu, S. W.; Sun, F. F.; Qi, H. Y.; Wu, H. F.; He, Y. H.; Liu, P.; Shi, R.; Zhang, J.; Kuc, A.; Kaiser, U.; Zhang, T. R.; Heine, T.; Wu, G.; Feng, X. L. Highly accessible and dense surface single metal FeN_4 active sites for promoting the oxygen reduction reaction. *Energy Environ. Sci.* **2022**, *15*, 2619−2628.

(13) Peng, B. S.; Liu, H. T.; Liu, Z. Y.; Duan, X. F.; Huang, Y. Toward rational design of single-atom catalysts. *J. Phys. Chem. Lett.* **2021**, *12*, 2837−2847.

(14) Li, Y.; Ji, Y. X.; Zhao, Y. J.; Chen, J. X.; Zheng, S. X.; Sang, X. H.; Yang, B.; Li, Z. J.; Lei, L. C.; Wen, Z. H.; Feng, X. L.; Hou, Y. Local spin-state tuning of iron single-atom electrocatalyst by S-coordinated doping for kinetics-boosted ammonia synthesis. *Adv. Mater.* **2022**, *34*, 2202240−2202249.

(15) Wang, M. R.; Yang, W. J.; Li, X. Z.; Xu, Y. S.; Zheng, L. R.; Su, C. L.; Liu, B. Atomically dispersed Fe-heteroatom (N, S) bridge sites anchored on carbon nanosheets for promoting oxygen reduction reaction. *ACS Energy Lett.* **2021**, *6*, 379−386.

(16) Zhang, Y.-L.; Dai, Y.-K.; Liu, B.; Gong, X.-F.; Zhao, L.; Cheng, F.; Cai, J.-J.; Zhou, Q.-Y.; Liu, B.; Wang, Z.-B. Vacuum vapor migration strategy for atom-nanoparticle composite catalysts boosting bifunctional oxygen catalysis and rechargeable Zn-air batteries. *J. Mater. Chem. A* **2022**, *10*, 3112−3121.

(17) Yuan, K.; Lützenkirchen-Hecht, D.; Li, L. B.; Shuai, L.; Li, Y. Z.; Cao, R.; Qiu, M.; Zhuang, X. D.; Leung, M. K. H.; Chen, Y. W.; Scherf, U. Boosting oxygen reduction of single iron active sites via geometric and electronic engineering: nitrogen and phosphorus dual coordination. *J. Am. Chem. Soc.* **2020**, *142*, 2404−2412.

(18) Jin, H. H.; Zhao, X.; Liang, L. H.; Ji, P. X.; Liu, B. S.; Hu, C. X.; He, D. P.; Mu, S. C. Sulfate ions induced concave porous S-N co-doped carbon confined FeC_x nanoclusters with Fe-N_4 sites for efficient oxygen reduction in alkaline and acid media. *Small* **2021**, *17*, 2101001−2101008.

(19) Sun, J.; Xue, H.; Lu, L. L.; Gao, M. B.; Guo, N. K.; Song, T. S.; Dong, H. L.; Zhang, J. W.; Wu, L. M.; Wang, Q. Atomic-level modulation of local coordination environment at Fe single-atom sites for enhanced oxygen reduction. *Appl. Catal. B-Environ.* **2022**, *313*, No. 121429.

(20) Chen, Z. Y.; Niu, H.; Ding, J.; Liu, H.; Chen, P.-H.; Lu, Y.-H.; Lu, Y.-R.; Zuo, W. B.; Han, L.; Guo, Y. Z.; Hung, S.-F.; Zhai, Y. M. Unraveling the origin of sulfur-doped Fe-N-C single-atom catalyst for enhanced oxygen reduction activity: effect of Iron spin-state tuning. *Angew. Chem. Int. Ed.* **2021**, *60*, 25404−25410.

(21) Zhang, J. T.; Zhang, M.; Zeng, Y.; Chen, J. S.; Qiu, L. X.; Zhou, H.; Sun, C. J.; Yu, Y.; Zhu, C. Z.; Zhu, Z. H. Single Fe atom on hierarchically porous S, N-codoped nanocarbon derived from porphyra enable boosted oxygen catalysis for rechargeable Zn-air batteries. *Small* **2019**, *15*, 1900307−1900317.

(22) Wang, Y.; Tang, Y-J.; Zhou, K. Self-adjusting activity induced by intrinsic reaction intermediate in Fe-N-C single-atom catalysts. *J. Am. Chem. Soc.* **2019**, *141*, 14115−14119.

(23) Zhao, K.-M.; Liu, S. Q.; Li, Y.-Y.; Wei, X. L.; Ye, G. Y.; Zhu, W. W.; Su, Y. K.; Wang, J.; Liu, H. T.; He, Z.; Zhou, Z.-Y.; Sun, S.-G. Insight into the mechanism of axial ligands regulating the catalytic

activity of Fe-N_4 sites for oxygen reduction reaction. *Adv. Energy Mater.* **2022**, *12*, 2103588−2103594.
(24) Yang, X.; Xia, D. S.; Kang, Y. Q.; Du, H. D.; Kang, F. Y.; Gan, L.; Li, J. Unveiling the axial hydroxyl ligand on Fe-N_4-C electrocatalysts and its impact on the pH-dependent oxygen reduction activities and poisoning kinetics. *Adv. Sci.* **2020**, *7*, 2000176−2000181.
(25) Wang, F. T.; Zhou, Y. P.; Lin, S.; Yang, L. J.; Hu, Z.; Xie, D. Q. Axial ligand effect on the stability of Fe-N-C electrocatalysts for acidic oxygen reduction reaction. *Nano Energy* **2020**, *78*, 105128−105133.
(26) Kresse, G.; Furthmüller, J. Efficient iterative schemes for ab initio total-energy calculations using a plane-wave basis set. *Phys. Rev. B* **1996**, *54*, 11169−11186.
(27) Kresse, G.; Furthmüller, J. Efficiency of ab-initio total energy calculations for metals and semiconductors using a plane-wave basis set. *Comput. Mater. Sci.* **1996**, *6*, 15−50.
(28) Kresse, G.; Joubert, D. From ultrasoft pseudopotentials to the projector augmented-wave method. *Phys. Rev. B* **1999**, *59*, 1758−1775.
(29) Perdew, J. P.; Burke, K.; Ernzerhof, M. Generalized gradient approximation made simple. *Phys. Rev. Lett.* **1996**, *77*, 3865−3868.
(30) Grimme, S.; Antony, J.; Ehrlich, S.; Krieg, H. A consistent and accurate ab initio parametrization of density functional dispersion correction (DFT-D) for the 94 elements H-Pu. *J. Chem. Phys.* **2010**, *132*, 154104−154123.
(31) Liu, K.; Fu, J. W.; Lin, Y. Y.; Luo, T.; Ni, G. H.; Li, H. M.; Lin, Z.; Liu, M. Insights into the activity of single-atom Fe-N-C catalysts for oxygen reduction reaction. *Nat. Commun.* **2022**, *13*, No. 2075.
(32) Wang, V.; Xu, N.; Liu, J.-C.; Tang, G.; Geng, W.-T. VASPKIT: A user-friendly interface facilitating high-throughput computing and analysis using VASP code. *Comput. Phys. Commun.* **2021**, *267*, 108033−108051.
(33) Nørskov, J. K.; Rossmeisl, J.; Logadottir, A.; Lindqvist, L.; Kitchin, J. R.; Bligaard, T.; Jónsson, H. Origin of the overpotential for oxygen reduction at a fuel-cell cathode. *J. Phys. Chem. B* **2004**, *108*, 17886−17892.
(34) Xie, X. Y.; Peng, L. S.; Yang, H. Z.; Waterhouse, G. I. N.; Shang, L.; Zhang, T. R. MIL-101-derived mesoporous carbon supporting highly exposed Fe single-atom sites as efficient oxygen reduction reaction catalysts. *Adv. Mater.* **2021**, *33*, 2101038−2101045.
(35) Liu, F.; Shi, L.; Song, S. F.; Ge, K.; Zhang, X. P.; Guo, Y. C.; Liu, D. Simultaneously engineering the coordination environment and pore architecture of metal-organic framework-derived single-atomic iron catalysts for ultraefficient oxygen reduction. *Small* **2021**, *17*, 2102425−2102435.
(36) Liu, H. M.; Huang, X. N.; Lu, Z. J.; Wang, T.; Zhu, Y. M.; Cheng, J. X.; Wang, Y.; Wu, D. L.; Sun, Z. Y.; Robertson, A. W.; Chen, X. X. Trace metals dramatically boost oxygen electrocatalysis of N-doped coal-derived carbon for zinc-air batteries. *Nanoscale* **2020**, *12*, 9628−9639.
(37) Han, Q. L.; Zhao, X. M.; Luo, Y. H.; Wu, L. L.; Sun, S. J.; Li, J. D.; Wang, Y. J.; Liu, H.; Chen, Z. W. Synergistic binary Fe-Co nanocluster supported on defective tungsten oxide as efficient oxygen reduction electrocatalyst in zinc-air battery. *Adv. Sci.* **2021**, *9*, 2104237−2104246.
(38) Han, Z. Y.; Li, X. Y.; Li, Q.; Li, H.; Xu, J.; Li, N.; Zhao, G.; Wang, X.; Li, H. L.; Li, S. D. Construction of the POMOF@ Polypyrrole composite with enhanced ion diffusion and capacitive contribution for high-performance lithium-ion batteries. *ACS Appl. Mater. Interfaces* **2021**, *13*, 6265−6275.
(39) Sarkar, S.; Biswas, A.; Siddharthan, E. E.; Thapa, R.; Dey, R. S. Strategic modulation of target-specifific isolated Fe,Co single-atom active sites for oxygen electrocatalysis impacting high power Zn-air battery. *ACS Nano* **2022**, *16*, 7890−7903.
(40) Yang, J.; Wang, X.; Li, B.; Ma, L.; Shi, L.; Xiong, Y. J.; Xu, H. X. Novel iron/cobalt-containing polypyrrole hydrogel-derived trifunctional electrocatalyst for self-powered overall water splitting. *Adv. Funct. Mater.* **2017**, *27*, 1606497−1606507.
(41) Guo, D. H.; Shibuya, R.; Akiba, C.; Saji, S.; Kondo, T.; Nakamura, J. Active sites of nitrogen-doped carbon materials for oxygen reduction reaction clarified using model catalysts. *Science* **2016**, *351*, 361−365.
(42) Peng, L. S.; Yang, J.; Yang, Y. Q.; Qian, F. R.; Wang, Q.; Sun-Waterhouse, D.; Shang, L.; Zhang, T. R.; Waterhouse, G. I. N. Mesopore-rich Fe-N-C catalyst with FeN_4−O−NC single atom sites delivers remarkable oxygen reduction reaction performance in alkaline media. *Adv. Mater.* **2022**, *34*, 2202544−2202553.
(43) Gan, G. Q.; Li, X. Y.; Fan, S. Y.; Yin, Z. F.; Wang, L.; Chen, G. H. Ultrathin Fe-N*x*-C single-atom catalysts with bifunctional active site for simultaneous production of ethylene and aromatic chlorides. *Nano Energy* **2021**, *80*, 105532−105539.
(44) Zhang, Z. Y.; Zhao, X. X.; Xi, S. B.; Zhang, L. L.; Chen, Z. X.; Zeng, Z. P.; Huang, M.; Yang, H. B.; Liu, B.; Pennycook, S. J.; Chen, P. Atomically dispersed cobalt trifunctional electrocatalysts with tailored coordination environment for flexible rechargeable Zn-air battery and self-driven water splitting. *Adv. Energy Mater.* **2020**, *10*, 2002896−2002906.
(45) Hou, C.-C.; Zou, L. L.; Sun, L. M.; Zhang, K. X.; Liu, Z.; Li, Y. W.; Li, C. X.; Zou, R. Q.; Yu, J. H.; Xu, Q. Single-atom iron catalysts on overhang-eave carbon cages for high-performance oxygen reduction reaction. *Angew. Chem., Int. Ed.* **2020**, *59*, 7384−7389.
(46) Wang, Y.-F.; Liang, Y. Y.; Wu, Y.-F.; Yang, J.; Zhang, X.; Cai, D. D.; Peng, X.; Kurmoo, M.; Zeng, M.-H. In situ pyrolysis tracking and real-time phase evolution: from a binary zinc cluster to supercapacitive porous carbon. *Angew. Chem., Int. Ed.* **2020**, *59*, 13232−13237.
(47) Wu, Q. L.; Jia, Y.; Liu, Q.; Mao, X.; Guo, Q.; Yan, X. C.; Zhao, J. P.; Liu, F. C.; Du, A. J.; Yao, X. D. Ultra-dense carbon defects as highly active sites for oxygen reduction catalysis. *Chem* **2022**, *8*, 2715−2733.
(48) Nagy, L.; Gajda, T.; Kürti, J.; Schrantz, K.; Burger, K. Spectroscopic studies of iron(III) complexes of D-saccharose and D-glucose in the solid state and in solution. *J. Radioanal. Nucl. Chem.* **1996**, *209*, 225−234.
(49) Yi, J.-D.; Xu, R.; Chai, G.-L.; Zhang, T.; Zang, K. T.; Nan, B.; Lin, H.; Liang, Y.-L.; Lv, J. Q.; Luo, J.; Si, R.; Huang, Y.-B.; Cao, R. Cobalt single-atoms anchored on porphyrinic triazine-based frameworks as bifunctional electrocatalysts for oxygen reduction and hydrogen evolution reactions. *J. Mater. Chem. A* **2019**, *7*, 1252−1259.
(50) Li, J. J.; Xia, W.; Tang, J.; Gao, Y.; Jiang, C.; Jia, Y. N.; Chen, T.; Hou, Z. F.; Qi, R. J.; Jiang, D.; Asahi, T.; Xu, X. T.; Wang, T.; He, J. P.; Yamauchi, Y. Metal-organic framework-derived graphene mesh: a robust scaffold for highly exposed Fe-N_4 active sites toward an excellent oxygen reduction catalyst in acid media. *J. Am. Chem. Soc.* **2022**, *144*, 9280−9291.
(51) Gao, J. J.; Hu, Y. X.; Wang, Y.; Lin, X. R.; Hu, K. L.; Lin, X.; Xie, G. Q.; Liu, X. J.; Reddy, K. M.; Yuan, Q. H.; Qiu, H.-J. MOF structure engineering to synthesize Co-N-C catalyst with richer accessible active sites for enhanced oxygen reduction. *Small* **2021**, *17*, 2104684−2104692.
(52) Liu, Y. R.; Liu, X. J.; Lv, Z. H.; Liu, R.; Li, L. H.; Wang, J. M.; Yang, W. X.; Jiang, X.; Feng, X.; Wang, B. Tuning spin state of Fe center by bridge bonded Fe-O-Ti ligands for enhanced oxygen reduction. *Angew. Chem. Int. Ed.* **2022**, *61*, No. e202117617.

https://doi.org/10.1021/acsami.3c03546
ACS Appl. Mater. Interfaces XXXX, XXX, XXX−XXX